Unconventional ferroelectricity in moiré heterostructures

Zhiren Zheng*,[1] Qiong Ma*†,[1,2] Zhen Bi,[1] Sergio de la Barrera,[1] Ming-Hao Liu,[3] Nannan Mao,[4,5] Yang Zhang,[1] Natasha Kiper,[1] Kenji Watanabe,[6] Takashi Taniguchi,[7] Jing Kong,[4] William A. Tisdale,[5] Ray Ashoori,[1] Nuh Gedik,[1] Liang Fu,[1] Su-Yang Xu,[1,8] and Pablo Jarillo-Herrero†[1]

[1]*Department of Physics, Massachusetts Institute of Technology, Cambridge, Massachusetts 02139, USA*

[2]*Department of Physics, Boston College, Chestnut Hill, Massachusetts 02467, USA*

[3]*Department of Physics, National Cheng Kung University, Tainan 70101, Taiwan*

[4]*Department of Electrical Engineering and Computer Science, Massachusetts Institute of Technology, Cambridge, Massachusetts 02139, United States*

[5]*Department of Chemical Engineering, Massachusetts Institute of Technology, Cambridge, Massachusetts 02139, United States*

[6]*Research Center for Functional Materials, National Institute for Materials Science, Namiki 1 -1, Tsukuba, Ibaraki 305 -0044, Japan*

[7]*International Center for Material Nanoarchitectonics, National Institute for Materials Science, Namiki 1 -1, Tsukuba, Ibaraki 305 -0044, Japan*

[8]*Department of Chemistry and Chemical Biology, Harvard University, Cambridge, Massachusetts 02138, USA*

(Dated: October 4, 2020)

* These authors contributed equally to this work.

† Corresponding authors: qiongm@mit.edu and pjarillo@mit.edu

Although all matter is composed of component particles, these particles can arrange themselves in various ways, giving rise to emergent phenomena that can be surprisingly rich and often cannot be understood by studying only the individual constituents. Discovering and understanding novel forms of emergence in quantum materials, especially in those where multiple degrees of freedom or energy scales are delicately balanced, is of great fundamental interest to condensed matter research [1, 2]. Here, we report on the surprising observation of emergent ferroelectricity in graphene-based moiré heterostructures. Ferroelectric materials exhibit an electrically-switchable electric dipole, which is usually formed by spatial separation between the averaged centers of positive and negative charge within the unit cell. Based on this, it is difficult to imagine graphene, a material composed only of carbon atoms, exhibiting ferroelectricity [3]. However, in this work, we indeed realize switchable ferroelectricity in Bernal-stacked bilayer graphene sandwiched between two hexagonal boron nitride (BN) layers. By introducing a moiré superlattice potential (via aligning bilayer graphene with the top and/or bottom BN crystals), we observe prominent and robust hysteretic behavior of the graphene resistance with an externally applied out-of-plane displacement field. Our systematic transport measurements reveal rich and striking response as a function of displacement field and electron filling, not previously observed in any 2D systems, and beyond the framework of conventional ferroelectrics. We further directly probe the ferroelectric polarization through a nonlocal monolayer graphene sensor. Our results suggest an unconventional, odd parity electronic ordering in the bilayer graphene/BN moiré system. This emergent moiré ferroelectricity may pave the way for ultrafast, programmable, and atomically thin carbon-based memory devices.

Discovering and classifying novel phases of matter has been a constant driving force throughout condensed matter research. For example, the recognition of spontaneous symmetry breaking has enabled the study and understanding of superconductors, magnets, and many other correlated electronic states under a unifying principle. The concepts of Berry phase and topology have led to novel topological phases including quantum spin Hall insulators, 3D topological insulators, and Weyl semimetals [4]. With these exciting advances, it is increasingly recognized that one of the next frontiers to discover new physics lies in

systems where electronic correlations, spontaneous symmetry breaking, and Berry phase are all at play [1, 2]. The realization of such systems with a variety of degrees of freedom in a delicate balance calls for unprecedented ability to design, engineer, and control electronic and symmetry properties of quantum materials.

In that sense, 2D moiré superlattices offer a uniquely suitable platform because they allow for a powerful, yet generic, way to induce electronic correlations into systems where interactions are otherwise not strong. For instance, monolayer graphene is a weakly interacting 2D semimetal. However, stacking one monolayer graphene on another at the magic angle ($\sim 1.1^\circ$) strongly modifies the electronic structure [5–7], giving rise to emergent phenomena [8, 9]. Current research, which has included a number of different moiré superlattices [10–21], has uncovered superconducting and magnetic states, among others. Superconductivity and magnetism correspond to the spontaneous breaking of gauge symmetry (charge conservation) and spin rotational symmetry, respectively. Another class of symmetries that plays an important role in both correlated physics and topology is the point group symmetries, such as inversion, mirror reflection, and rotation. The spontaneous breaking of point group symmetries can give rise to a wide range of novel electronic orders [22–25]. Moreover, these electronic orders are predicted to serve as precursors to unconventional superconducting pairing [26] or novel magnetism [27]. However, apart from a few studies reporting evidence of nematicity in magic-angle graphene [28–30] and the observation of the quantum anomalous Hall effect in BN-aligned magic-angle and ABC graphene [11, 12, 14, 31], the role of point group symmetries in moiré systems remains largely under-explored.

Here, we study Bernal-stacked bilayer graphene [32] aligned with BN, a simple yet rich moiré system where electronic correlations, Berry phase, and point group symmetries (such as inversion symmetry) are simultaneously important. In Bernal-stacked bilayer graphene, the unit cell consists of two inversion pairs (Fig. 1**a**). The space inversion symmetry is effectively equivalent to the layer degeneracy. The application of an external out-of-plane displacement field breaks the layer degeneracy and gives rise to a layer polarization in the quantum wavefunction near the band edges, and hence a non-zero Berry curvature (Fig. 1**b**). Such Berry curvature lies at the heart of the topological valley transport as well as chiral optical and excitonic properties in bilayer graphene [33–37]. Because of this unique electronic structure, theory has long predicted a wide range of spontaneous electronic order in pristine bilayer graphene [32]. Under high magnetic fields at very low temperatures, experiments

have indeed revealed a number of broken symmetry phases in the Landau levels [38, 39]. On the other hand, in the absence of a magnetic field, interesting experimental results suggested electronic correlations [40–43], but the effects remain relatively subtle even at very low temperatures with ultra-high quality samples, and their exact nature remains unsettled. Here, we put such chiral, quadratic gapless fermions that are protected by the layer degeneracy onto a moiré superlattice potential (Fig. 1**c**), to search for correlation-driven spontaneous symmetry breaking. In the following, we report on the observation of emergent unconventional ferroelectricity in this system.

We have fabricated high quality, BN-encapsulated, dual-gated bilayer graphene devices, as shown in Fig. 1**c**. This allows us to independently tune the externally applied charge density, $n_{\rm ext}$, and the out-of-plane electric displacement field, $D_{\rm ext}$ through experimental control of the gate voltages (Methods). The moiré superlattice potential is introduced by the rotational alignment between the bilayer graphene and the encapsulating BN flakes, which plays a crucial role in the observed ferroelectricity. Such rotational alignment was achieved by aligning the straight edges of the bilayer graphene flake and one of the BN flakes. The other degree of freedom is the relative angle between the top and bottom BN flakes. In Devices H2 and H4, the top and bottom BN flakes have a relative angle of $\sim$ 30 degrees and $\sim$ 0 degrees, respectively; in Devices H1 and H3, the top and bottom BN flakes have a relative angle of $\sim$ 20 degrees (Methods). Devices H2 and H4 exhibit dramatic hysteretic responses to the externally applied displacement field, whereas hysteresis in Devices H1 and H3 is relatively weaker.

Ferroelectric response in the BLG/BN moiré system

In the main text, we focus on the hysteretic characteristics of Devices H2 and H4. All the data shown were taken at T = 4 K, unless otherwise noted. In Figs. 1**d**, the normal bilayer graphene (Device N0) exhibits no hysteresis between forward and backward $V_{\rm BG}$ scans, whereas Device H2 and Device H4 (Figs. 1**e,f**) show significant hysteresis. It is interesting to note that the resistance hysteresis loops for Devices H2 and H4 have the opposite sequence in terms of whether the resistance peak appears in an advanced or a retarded fashion, pointing to the unconventional nature of the ferroelectricity (see SI. III).

To further illustrate this behavior, we now systematically show the hysteretic transport behavior of Device H4 by presenting the four-probe resistance measured as a function of top and bottom gate voltages ($V_{\rm TG}$ and $V_{\rm BG}$). (1) In the range of $V_{\rm TG}$ from -8 to +8 V and $V_{\rm BG}$

from -10 to +10 V (Fig. 2**a**), Device H4 behaves almost like normal bilayer graphene with the gapless point at $V_{\mathrm{TG}} = V_{\mathrm{BG}} = 0$. (2) We reverse the scan direction of V_{BG} and scan V_{BG} from +10 to -10 V. Identical normal bilayer graphene behavior is observed. (3) However, when we further extend the range of V_{BG} downward (Fig. 2**b**), the resistance peak ridge suddenly turns to be almost parallel to the V_{BG} axis upon reaching $V_{\mathrm{BG}} \approx -15$ V. In other words, in this regime, the device *appears* to behave as if the bottom gate "stops working" whereas the top gate still functions normally. In the following, we refer to such a phenomenon as LSAS ("layer-specific anomalous screening") because the phenomenon suggests that the electric field from a specific gate appears to be anomalously screened (SI. III). (4) Upon reaching $V_{\mathrm{BG}} = -20$ V, we reverse again the scanning direction of V_{BG} (Fig. 2**c**). Equally strikingly, the LSAS behavior immediately stops, and normal bilayer graphene behavior is recovered. (5) However, once we reach far enough on the opposite side of the gapless point, we enter another LSAS regime (Fig. 2**c**). (6) At this point, if we reverse the scanning direction of V_{BG} again, the resistance immediately follows a normal bilayer graphene behavior and switches to the LSAS behavior after a certain distance across the gapless point (Fig. 2**d**). As such, the resistance peak lines for the two scanning directions form a parallelogram (Figs. 2**e-g** and Extended Data Fig. 2). In other words, we observe very prominent hysteretic behavior depending on the bottom gate scanning direction. However, no anomalous screening is observed along the top gate direction (SI.V.3). A complete set of equivalent measurements for Device H2 is shown in Extended Data Figs. 3-4, with similarly dramatic hysteretic characteristics.

We summarize a few key observations in Figs. 2**a-g**: (1) Two particular electric displacement fields on opposite sides of the gapless point (D_1 and D_2 in Figs. 2**e-f**) separate the normal bilayer graphene behavior region and the LSAS region. When scanning upward with increasing V_{BG}, the peak line becomes parallel to the V_{BG} axis upon reaching D_1 (Fig. 2**e**). The same applies for D_2 when scanning downward with decreasing V_{BG} (Fig. 2**f**). Similar behavior is observed when the bottom gate is used as the fast scan axis (SI.V.3). (2) Interestingly, D_1 and D_2 appear to be fixed with respect to the gapless point, whose position in the parameter space of $(V_{\mathrm{TG}}, V_{\mathrm{BG}})$ can vary depending on the scanning history (Extended Data Fig. 2).

Hall measurement along D_{ext}

We now change the scan variables to D_{ext} (fast axis) and n_{ext} (slow axis) by sweeping

V_{TG} and V_{BG} simultaneously. Consistent results are observed, as shown in Fig. 2**h,i**. The transverse resistance R_{xy} directly measures the (mobile) charge density $n_{\mathrm{H}} = \frac{B}{eR_{xy}}$, which therefore allows us to probe the conductive regimes that appear less prominent in the resistance maps. In Fig. 2**j**, for the forward scan (red curve), n_{H} shows that the system is electron-doped, and the mobile charge density remains roughly unchanged for $D_{\mathrm{ext}} < D_1$. However, for $D_{\mathrm{ext}} > D_1$, n_{H} starts to deviate, consistent with the LSAS observed in resistance, and, as a result, D_{ext} can change the mobile charge density of the system. We now reverse D_{ext} to scan backward. As described above, the moment we reverse the scan direction, the LSAS behavior stops, so n_{H} (blue curve) maintains a constant value until we reach D_2. We show n_{H} at three fixed n_{ext} values (Figs. 2**j-l**). Interestingly, n_{H} always starts to change at the same D_{ext} values and with the same Δn_{H}. Therefore, our Hall measurements show that D_1 and D_2 are the same irrespective of n_{ext} within our accessible scan range. Similar Hall measurements were also conducted in Device H2, as shown in Extended Data Fig. 5. We note that both the LSAS behavior and the ability of D_{ext} to change the mobile charge density are very surprising and not observed in other 2D devices. We will return to this point in the latter part of the paper.

Measurement of remnant polarization

We now show how the hysteretic resistance map in the $(D_{\mathrm{ext}}, n_{\mathrm{ext}})$ parameter space can be used to visualize and to measure a switchable out-of-plane spontaneous polarization, *i.e.*, ferroelectric ordering. The gapless band touching is only realized when the top and bottom layers are degenerate, which implies an absence of an electrical displacement field across the two layers. In the presence of ferroelectric ordering, the interlayer displacement field has two contributions, the field induced by gating ($\sim D_{\mathrm{ext}}$) and the internal electric field arising from the built-in ferroelectric polarization (P). As such, the gapless point is only realized when the externally induced and internal fields cancel each other out, *i.e.*, zero total interlayer displacement field (see SI.IV for further discussion). As shown in Fig. 3**a**, the gapless points that appear in the two normal bilayer regimes (horizontal resistance peak lines) are located at nonzero and opposite D_{ext} values, demonstrating the existence of a switchable, remnant polarization. From this analysis, we can directly read out $\Delta D_{ext}/\varepsilon_0$ from Fig. 3**a** and convert into the remnant polarization by simply multiplying ε_0. For H4, $\Delta P_{\mathrm{H4}} = P_{\mathrm{forward}} - P_{\mathrm{backward}} = +0.05\ \mu\mathrm{C{\cdot}cm^{-2}}$. Interestingly, the remnant polarization scales with the range of the displacement field, which is further explored in SI.V.3. Additionally,

we probe the polarization of Device H4 independently by a nonlocal monolayer graphene sensor, a technique recently demonstrated in Ref. [44], and we obtain consistent results (Methods). Similarly, Device H2 also shows prominent hysteresis that forms a parallelogram (Fig. 3**b**). In Device H2, it is the top gate that *appears* to be "not working" in the switching regime, which is manifested as the opposite tilting direction of the parallelogram in Fig. 3**b** (see more data on Device H2 in SI.V.2). Using the same method, we obtain $\Delta P_{\mathrm{H2}} = P_{\mathrm{forward}} - P_{\mathrm{backward}} = -0.18\ \mu\mathrm{C{\cdot}cm^{-2}}$ for Device H2. Intriguingly, Device H4 and Device H2 have opposite remnant electrical polarization (Insets of Figs. 3**a-b**). Consequently, the $P-D_{\mathrm{ext}}$ loop in H4 is clockwise while the $P-D_{\mathrm{ext}}$ loop in H2 is contour-clockwise as a result of their opposite sequence between the normal bilayer graphene and LSAS behavior (see SI. III). In fact, the opposite behaviors have already been suggested by the opposite sequences of the resistance switching shown in Figs. 1**e-f**. A conventional ferroelectric material has a counter-clockwise $P-E$ loop. So in this sense, the behavior of Device H4 is highly unusual. Moreover, here we observe both, opposite behaviors in Device H4 and H2. We provide a possible microscopic picture below.

A microscopic theoretical picture

Our observation of strong hysteresis and LSAS phenomena provide an incentive to understand the underlying mechanism. Our systematic measurements and analyses of the hysteretic and control devices strongly suggest that an extrinsic charge trapping mechanism is unlikely to be responsible, and, in addition, the ferroelectric behavior cannot be well-explained based on a lattice model in the framework of conventional ferroelectrics (Methods). Instead, our theoretical analyses and experimental observations indicate an intrinsic origin and an unconventional nature of the reported ferroelectricity.

We now provide an intuitive theoretical picture based on interaction-induced interlayer charge transfer which captures the dominant features in our data [45]. We note, however, that further theoretical work will be required to confirm the plausibility of this picture. First, we highlight important properties of the single-particle electronic structure of the bilayer graphene/BN moiré system. As mentioned above, normal bilayer graphene (misaligned to BN) has a quadratic band dispersion. An external displacement field gaps out the quadratic band touching and flattens the dispersion near the gap edge. Importantly, while states in the vicinity of the gap edge become layer polarized, states away from it remain layer degenerate (Figs. 3**c,d**). In the case of BLG aligned to BN, because of the small moiré wavevector k_{m},

it is possible for the entire low-energy moiré band to become highly layer polarized (Fig. 3**e**) at a large enough displacement field. In real space, this means that electrons occupying a moiré band at low energy are located on a specific layer. In momentum space, this means that the low-energy moiré band will become increasingly flat. Without loss of generality, let us consider a large positive displacement field. Then the highest moiré valence band and the lowest moiré conduction band will be largely polarized to the bottom and top layers, respectively (Fig. 3**e**).

Second, we now consider the effect of correlations. As one increases the displacement field, the bands become increasingly flat and layer polarized. The kinetic energy becomes quenched, making the effect of correlations (*e.g.*, on-site Coulomb repulsion) more significant. This gate-tunable correlation effect is a unique property of bilayer graphene, where band gap formation through an external electric field allows modification of the bandwidth, effective mass, and hence correlation strength (SI.IV). Based on our data, we assume that the on-site repulsion in the bottom layer is the relevant one in Device H4. This layer asymmetry translates into the asymmetry between the moiré valence and conduction bands due to the electronic layer polarization. In this particular discussion ($D_{ext} > 0$), the correlation effect (on-site repulsion U) dominates in the moiré valence band. There may exist a critical displacement field above which the on-site repulsion U in the bottom layer (valence band) is sufficiently strong that the moiré valence band splits into lower and upper Hubbard bands (Fig. 3**f**). Because U is larger than the band gap Δ, it is energetically more favorable for electrons to occupy the moiré conduction band rather than the upper Hubbard band. This leads to a transfer of electrons from the valence band (bottom layer) to the moiré conduction band (top layer), which is accompanied by a change of the polarization. It is important to note that this polarization generated by the interlayer charge transfer is actually in the direction opposite to the externally applied positive displacement field. Further, this process is hysteretic, because increasing V_{BG} triggers the interlayer charge transfer whereas decreasing V_{BG} does not. Specifically, increasing V_{BG} adds electrons to the fully polarized upper Hubbard band (the bottom layer). This process is energetically unfavorable due to strong Coulomb repulsion. As a result, increasing V_{BG} does not introduce electrons to the graphene from the ground; rather, electrons are transferred from the bottom layer to the top layer within the graphene, leading to the observed LSAS behavior. In contrast, decreasing V_{BG} removes electrons from the graphene system, which is energetically allowed. Therefore,

when we reverse the scanning direction to decrease V_{BG}, the interlayer charge transfer does not occur; the LSAS stops and normal bilayer graphene behavior appears. Using the fact that the interlayer charge transfer gives rise to a polarization that is in the opposite direction to the external displacement field and that, the moment when we reverse the scanning direction to decrease V_{BG}, the LSAS stops and the normal bilayer graphene behavior appears, one can find that a clockwise $P - D_{\mathrm{ext}}$ loop is naturally derived. This process is energetically possible due to the ability of D_{ext} to change the mobile charge density, meaning that our system is not an isolated system and it exchanges particles with the environment, unlike conventional ferroelectric materials.

With the layer-specific moiré flat bands and interlayer charge transfer picture, the ferroelectricity and LSAS behavior in Devices H4 and H2 can both be understood (see Methods and SI.III). Meanwhile, it is interesting to note that a spontaneous interlayer charge transfer has been observed in the GaAs double layer system [46]. Although the above picture may capture dominant features in our data, we wish to emphasize that further experiments are needed to fully understand the observed ferroelectricity.

Robustness of the ferroelectric switching

We now present further systematic measurements to demonstrate the robustness of the ferroelectric switching. In Fig. 4**a**, we repeat the same hysteresis loop 20 consecutive times. All 20 scans fall exactly onto each other. Such remarkable reproducibility confirms the intrinsic nature of our observations. In Fig. 4**b**, we perform five consecutive D_{ext} scans along alternating forward and backward directions with different ranges while keeping $n_{\mathrm{ext}} = 0$: (1) We start from zero displacement field and scan D_{ext} forward (the green curve), as D_{ext} surpasses D_1, the LSAS occurs and we observe a conductance dip (resistance peak) that corresponds to cutting through the right edge of the parallelogram in Fig. 3**a**. (2) As soon as we turn back (pink curve), both gates function normally. Therefore, the system immediately follows a constant conductance curve. Once we reach $D_{\mathrm{ext}} = 0$ we stop. (3) We then scan again forward (black curve). Since the pink curve did not reach D_2, the black curve exactly follows the pink curve. (4) We turn around to scan backward (blue curve), this time going below D_2. As D_{ext} surpasses D_2, the system again enters the LSAS regime and we observe a resistance peak that corresponds to cutting through the left edge of the parallelogram in Fig. 3**a**. (5) Turning back to scan forward, both gates work normally until we reach D_1 and the behavior is identical to the green curve. These scans confirm that the

switching behavior in H4 is robustly triggered by reaching the LSAS regime.

Moving forward, our observations suggest many exciting possibilities. In terms of fundamental physics, it would be interesting to study many other bilayer 2D crystals under a moiré superlattice potential. In fact, the methodology applied here may be generalized to create ferroelectricity in a wide range of naturally non-polar 2D crystals. Since the ferroelectric instability is intrinsically odd-parity, its introduction into magnetic or superconducting systems may induce exotic magneto-electric coupling [27] or odd-parity Cooper pairing [26]. The unconventional ferroelectricity can also enable a number of novel nonlinear optical responses. In terms of applications, by writing domains with piezoelectric force microscopy, one can design controllable topological electrical circuits [34–36]. Moreover, our systems can be used as high-performance memory devices due to the strong hysteresis, large on-off ratio, and remarkable robustness. More significantly, the promise of electronically-driven switching may enable next-generation memory components with potentially ultrafast operation speeds.

[1] Keimer, B. & Moore, J. E. The physics of quantum materials. *Nature Phys.* **13**, 1045–1055 (2017).

[2] Tokura, Y., Kawasaki, M. & Nagaosa, N. Emergent functions of quantum materials. *Nature Phys.* **13**, 1056–1068 (2017).

[3] Castro Neto, A. H., Guinea, F., Peres, N. M. R., Novoselov, K. S. & Geim, A. K. The electronic properties of graphene. *Rev. Mod. Phys.* **81**, 109–162 (2009).

[4] Armitage, N. P., Mele, E. J. & Vishwanath, A. Weyl and dirac semimetals in three-dimensional solids. *Rev. Mod. Phys.* **90**, 015001 (2018).

[5] Morell, E. S., Correa, J., Vargas, P., Pacheco, M. & Barticevic, Z. Flat bands in slightly twisted bilayer graphene: Tight-binding calculations. *Physical Review B* **82**, 121407 (2010).

[6] Li, G. *et al.* Observation of van hove singularities in twisted graphene layers. *Nature Phys.* **6**, 109–113 (2010).

[7] Bistritzer, R. & MacDonald, A. H. Moiré bands in twisted double-layer graphene. *PNAS* **108**, 12233–12237 (2011).

[8] Cao, Y. *et al.* Unconventional superconductivity in magic-angle graphene superlattices. *Nature* **556**, 43–50 (2018).

[9] Cao, Y. *et al.* Correlated insulator behaviour at half-filling in magic-angle graphene superlattices. *Nature* **556**, 80–84 (2018).

[10] Yankowitz, M. *et al.* Tuning superconductivity in twisted bilayer graphene. *Science* **363**, 1059–1064 (2019).

[11] Sharpe, A. L. *et al.* Emergent ferromagnetism near three-quarters filling in twisted bilayer graphene. *Science* **365**, 605–608 (2019).

[12] Serlin, M. *et al.* Intrinsic quantized anomalous hall effect in a moiré heterostructure. *Science* **367**, 900–903 (2020).

[13] Chen, G. *et al.* Evidence of a gate-tunable Mott insulator in a trilayer graphene moiré superlattice. *Nature Phys.* **15**, 237–241 (2019).

[14] Chen, G. *et al.* Tunable correlated chern insulator and ferromagnetism in a moiré superlattice. *Nature* **579**, 56–61 (2020).

[15] Burg, G. W. *et al.* Correlated insulating states in twisted double bilayer graphene. *Phys. Rev. Lett.* **123**, 197702 (2019).

[16] Liu, X. *et al.* Spin-polarized correlated insulator and superconductor in twisted double bilayer graphene. *Nature* **583**, 221–225 (2019).

[17] Cao, Y. *et al.* Tunable correlated states and spin-polarized phases in twisted bilayer–bilayer graphene. *Nature* **583**, 215–220 (2020).

[18] Shen, C. *et al.* Correlated states in twisted double bilayer graphene. *Nature Phys.* 1–6 (2020).

[19] Wang, L. *et al.* Magic continuum in twisted bilayer WSe_2. *arXiv:* **1910.12147** (2019).

[20] Regan, E. C. *et al.* Mott and generalized wigner crystal states in WSe_2/WS_2 moiré superlattices. *Nature* **579**, 359–363 (2020).

[21] Tang, Y. *et al.* Simulation of hubbard model physics in WSe_2/WS_2 moiré superlattices. *Nature* **579**, 353–358 (2020).

[22] Nandkishore, R. & Levitov, L. Dynamical screening and excitonic instability in bilayer graphene. *Phys. Rev. Lett.* **104**, 156803 (2010).

[23] Fradkin, E., Kivelson, S. A., Lawler, M. J., Eisenstein, J. P. & Mackenzie, A. P. Nematic fermi fluids in condensed matter physics. *Annu. Rev. Condens. Matter Phys.* **1**, 153–178 (2010).

[24] Fu, L. Parity-breaking phases of spin-orbit-coupled metals with gyrotropic, ferroelectric, and

multipolar orders. *Phys. Rev. Lett.* **115**, 026401 (2015).

[25] Fernandes, R. M. & Venderbos, J. W. Nematicity with a twist: rotational symmetry breaking in a moiré superlattice. *arXiv:* **1911.11367** (2019).

[26] Kozii, V. & Fu, L. Odd-parity Superconductivity in the Vicinity of Inversion Symmetry Breaking in Spin-Orbit-Coupled systems. *Phys. Rev. Lett.* **115**, 207002 (2015).

[27] Mishra, A. & Lee, S. Topological multiferroic phases in the extended Kane-Mele-Hubbard model in the Hofstadter regime. *Phys. Rev. B* **98**, 235124 (2018).

[28] Cao, Y. *et al.* Nematicity and competing orders in superconducting magic-angle graphene. *arXiv:* **2004.04148** (2020).

[29] Jiang, Y. *et al.* Charge order and broken totational symmetry in magic angle twisted bilayer graphene. *Nature* **573**, 91–95 (2019).

[30] Choi, Y. *et al.* Imaging electronic correlations in twisted bilayer graphene near the magic angle. *Nature Phys.* **15**, 1174–1180 (2019).

[31] Zhang, Y.-H., Mao, D., Cao, Y., Jarillo-Herrero, P. & Senthil, T. Nearly flat chern bands in moiré superlattices. *Physical Review B* **99**, 075127 (2019).

[32] McCann, E. & Koshino, M. The electronic properties of bilayer graphene. *Reports on Progress in Physics* **76**, 056503 (2013).

[33] Li, J., Martin, I., Büttiker, M. & Morpurgo, A. F. Topological origin of subgap conductance in insulating bilayer graphene. *Nature Physics* **7**, 38 (2011).

[34] Ju, L. *et al.* Topological valley transport at bilayer graphene domain walls. *Nature* **520**, 650–655 (2015).

[35] Sui, M. *et al.* Gate-tunable topological valley transport in bilayer graphene. *Nature Phys.* **11**, 1027–1031 (2015).

[36] Shimazaki, Y. *et al.* Generation and detection of pure valley current by electrically induced Berry curvature in bilayer graphene. *Nature Phys.* **11**, 1032–1036 (2015).

[37] Ju, L. *et al.* Tunable excitons in bilayer graphene. *Science* **358**, 907–910 (2017).

[38] Maher, P. *et al.* Evidence for a spin phase transition at charge neutrality in bilayer graphene. *Nature Phys.* **9**, 154–158 (2013).

[39] Hunt, B. *et al.* Direct measurement of discrete valley and orbital quantum numbers in bilayer graphene. *Nature Commun.* **8**, 948 (2017).

[40] Weitz, R. T., Allen, M., Feldman, B., Martin, J. & Yacoby, A. Broken-symmetry states in

doubly gated suspended bilayer graphene. *Science* **330**, 812–816 (2010).

[41] Bao, W. *et al.* Evidence for a spontaneous gapped state in ultraclean bilayer graphene. *PNAS* **109**, 10802–10805 (2012).

[42] Freitag, F., Trbovic, J., Weiss, M. & Schönenberger, C. Spontaneously gapped ground state in suspended bilayer graphene. *Phys. Rev. Lett.* **108**, 076602 (2012).

[43] Nam, Y., Ki, D.-K., Soler-Delgado, D. & Morpurgo, A. F. A family of finite-temperature electronic phase transitions in graphene multilayers. *Science* **362**, 324–328 (2018).

[44] Fei, Z. *et al.* Ferroelectric switching of a two-dimensional metal. *Nature* **560**, 336–339 (2018).

[45] Zhang, Y., Yuan, N. F. & Fu, L. Moiré quantum chemistry: charge transfer in transition metal dichalcogenide superlattices. *arXiv:* **1910.14061** (2019).

[46] Katayama, Y., Tsui, D., Manoharan, H., Parihar, S. & Shayegan, M. Charge transfer at double-layer to single-layer transition in double-quantum-well systems. *Phys. Rev. B* **52**, 14817–14824 (1995).

Acknowledgement: We thank D. Bandurin, V. Fatemi, L. Levitov, Y. Lin, J. Mundy, R. Ramesh, J. Sanchez-Yamagishi, H. Shen, J. Song, S. Todadri, A. Vishwanath, and N. Yuan for discussions. We also thank T. Dinh for initial efforts on this project. Work in the PJH group was supported by the US DOE, BES Office, Division of Materials Sciences and Engineering under Award DE-SC0001819 (device fabrication and transport measurements), the Center for the Advancement of Topological Semimetals, an Energy Frontier Research Center funded by the U.S. Department of Energy Office of Science, through the Ames Laboratory under contract DE-AC02-07CH11358 (data analysis), and the Gordon and Betty Moore Foundation's EPiQS Initiative through Grant GBMF9643 to PJH. The development of new nanofabrication and characterization techniques enabling this work has been supported by the US DOE Office of Science, BES, under award DE-SC0019300. Partial support for measurement and characterization training was supported through AFOSR grant FA9550-16-1-0382. This work made use of the Materials Research Science and Engineering Center Shared Experimental Facilities supported by the National Science Foundation (NSF) (Grant No. DMR-0819762). NG and SYX acknowledge support from DOE, BES DMSE (data taking and analysis), and National Science Foundation under Grant No. DMR-1809815 (manuscript writing). KW and TT acknowledge support from the Elemental Strategy Initiative conducted by the MEXT, Japan, Grant Number JPMXP0112101001, JSPS KAK-

ENHI Grant Numbers JP20H00354 and the CREST(JPMJCR15F3), JST. RA (capacitance measurements), ZB, YZ, and LF (theory) acknowledge support from NSF Science and Technology Center for Integrated Quantum Materials grant DMR-1231319. MHL was supported by Taiwan Ministry of Science and Technology (MOST) under Grant No.107-2112-M-006-004-MY3. NM and JK acknowledge the support by the U.S. Department of Energy (DOE), Office of Science, Basic Energy Sciences (BES) under Award DE-SC0020042.

Author contributions: QM and SYX conceived the idea and experiment. ZZ fabricated devices, performed transport measurements, and analyzed data under the supervision of QM and PJH. SB performed capacitance measurements with the help of ZZ under the supervision of RA. ZB, YZ, and NK performed theoretical modeling and band structure calculations under the supervision of SYX, QM, NG, and LF. MHL performed the simulation of the transport behaviors for the hysteretic devices. NM performed second-harmonic generation measurements of BN flakes under the supervision of JK and WAT. KW and TT grew the bulk BN single crystals. All authors discussed the results and wrote the manuscript.

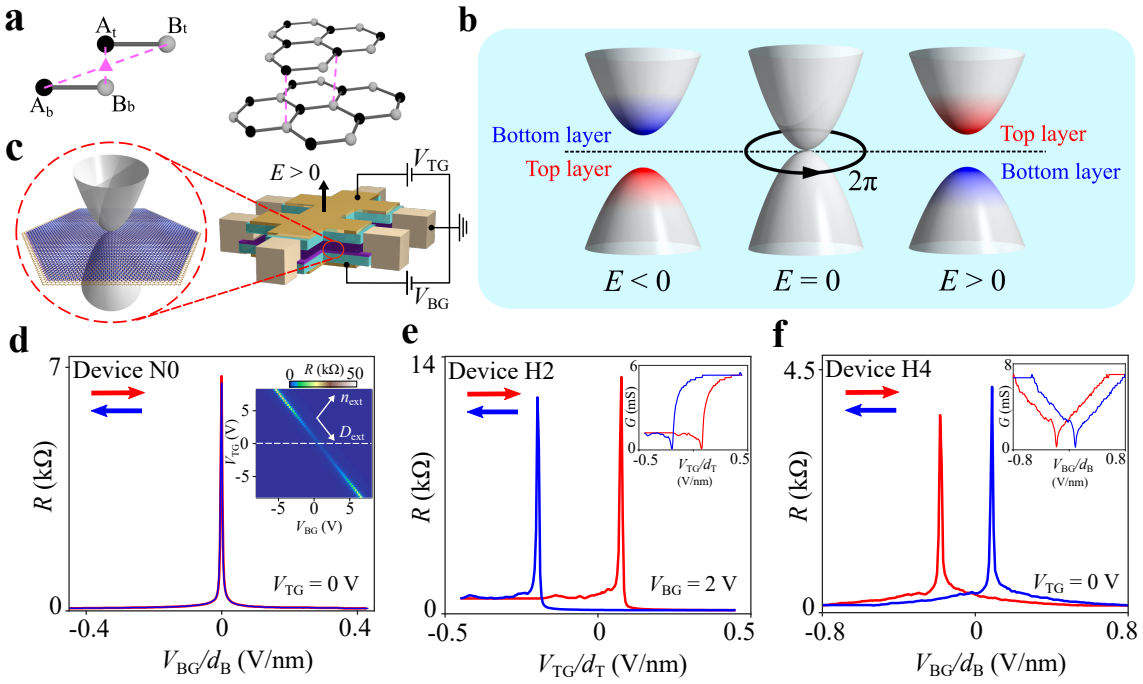

FIG. 1: **Bilayer graphene/BN moiré superlattice: quadratic, chiral fermions on a moiré potential. a,** Lattice structure of Bernal-stacked bilayer graphene. The triangle marks its inversion center. **b,** Schematic illustration of the band dispersion and layer polarization of the low-energy electronic states of pristine bilayer graphene at different interlayer electric fields. **c,** Schematic of our BN-encapsulated bilayer device with top ($V_{\rm TG}$) and bottom ($V_{\rm BG}$) gates. The black arrow identifies the positive electric field direction. Left panel: schematic illustration of the bilayer graphene/BN moiré superlattice pattern. One-side alignment is shown with an enlarged lattice mismatch for clarity. **d-f,** Four-probe resistance for a normal bilayer graphene Device N0 (**d**) and the hysteretic Device H2 (**e**) and Device H4 (**f**). The x axis $V_{\rm BG}(V_{\rm TG})$ is normalized by the bottom BN thickness $d_{\rm B}(d_{\rm T})$. The forward and backward scans are shown in red and blue, respectively. The inset of (**d**) is the dual-gate map of the four-probe resistance for the normal bilayer graphene. The insets of (**e**) and (**f**) are the conductance plots.

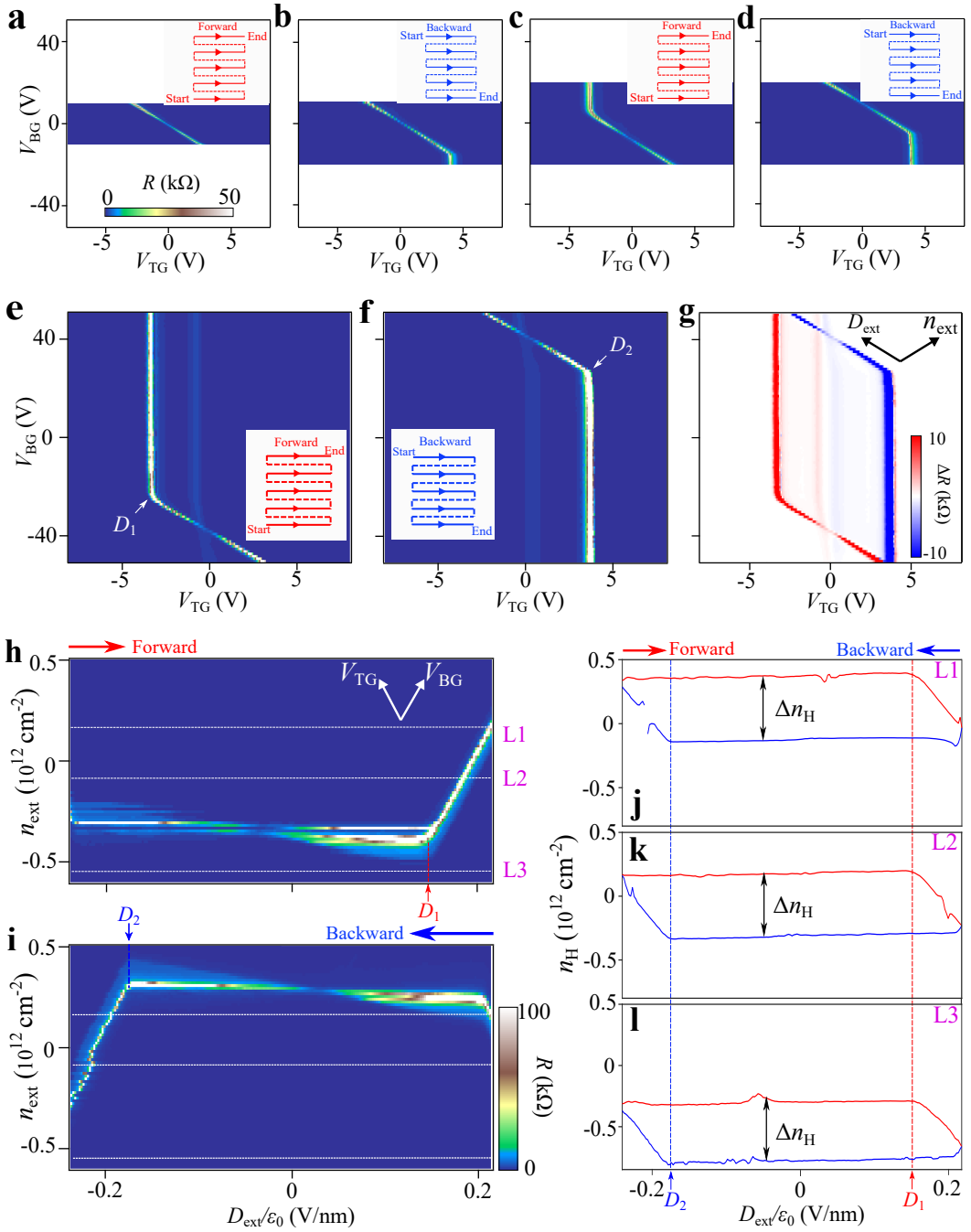

FIG. 2: **Hysteretic transport behavior for Device H4. a-d,** The four-probe longitudinal resistance as a function of the top gate voltage, V_{TG}, and the bottom gate voltage, V_{BG}. Insets: The "zigzag" patterns illustrate how the data are taken. "Start" ("End") denotes the starting (ending) point for each dual-gate map. During these measurements, V_{TG} is swept as the fast scan axis and V_{BG} is swept as the slow scan axis. At a fixed V_{BG}, we scan V_{TG} from -8 V to +8 V while recording data (solid lines) and then ramp back to -8 V continuously without recording (dashed lines). We change V_{BG} by a small step and scan V_{TG} back and forth again. Only the data collected along the solid lines are shown. **e-f,** Forward and backward scans for V_{BG} swept between -50 to 50 V. **g,** The difference between resistance measured in (**e**) and (**f**). **h-i,** The resistance measured while sweeping the externally applied displacement field D_{ext} in the forward (**h**) and backward (**i**) direction at each fixed carrier density n_{ext}. The carrier density scan direction is from the negative to positive values. **j-l,** Carrier density (n_H) extracted from Hall measurements along the lines denoted in (**h**) and (**i**).

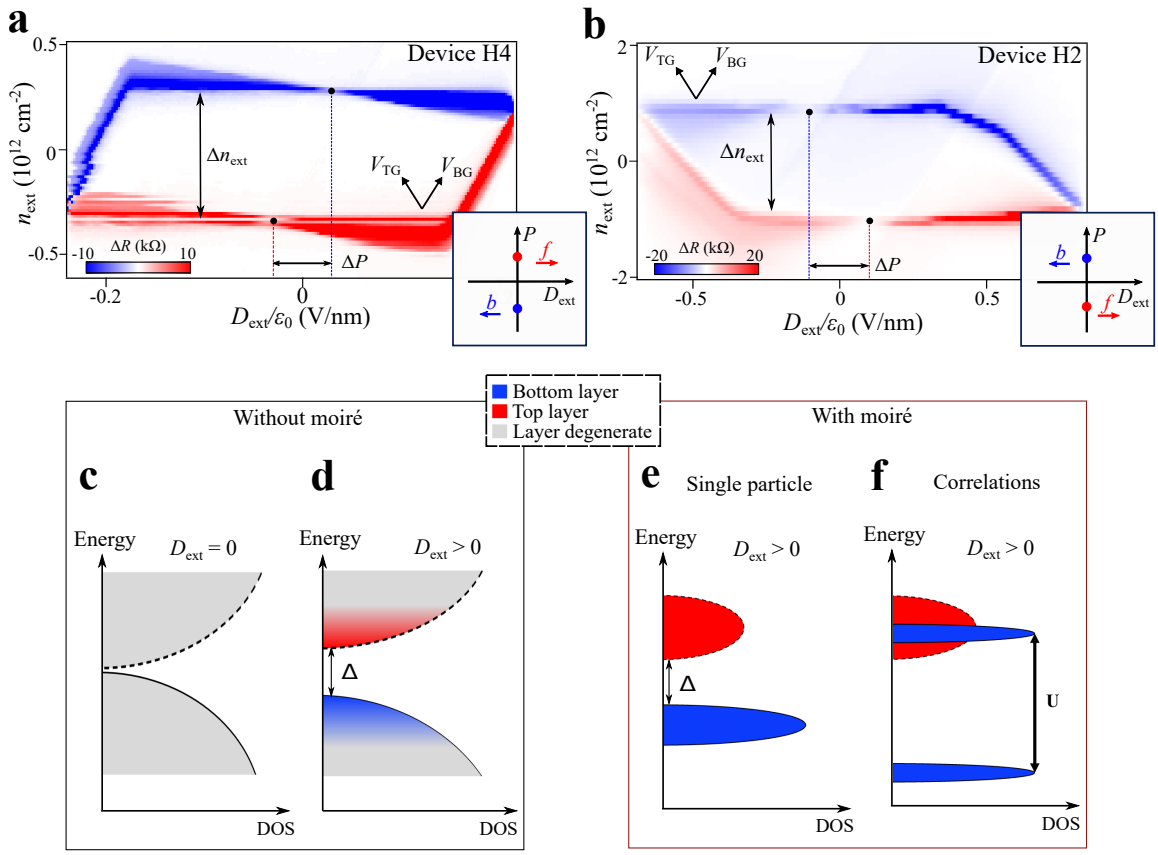

FIG. 3: **Measuring the out-of-plane electric polarization and a possible microscopic picture based on interlayer charge transfer. a,** The resistance difference between Figs. 2**h** and **i**. $\Delta P_{H4} = P_{forward} - P_{backward} = +0.05\ \mu C{\cdot}cm^{-2}$. **b,** Same as panel (**a**) but for Device H2. $\Delta P_{H2} = P_{forward} - P_{backward} = -0.18\ \mu C{\cdot}cm^{-2}$. **c-f,** Schematics of energy vs. density of states under four scenarios: pristine bilayer graphene without moiré superlattice at **c,** zero external displacement field and at **d,** positive external displacement field. Device H4 at positive external displacement field **e,** in a single particle picture and **f,** with consideration of correlation effect.

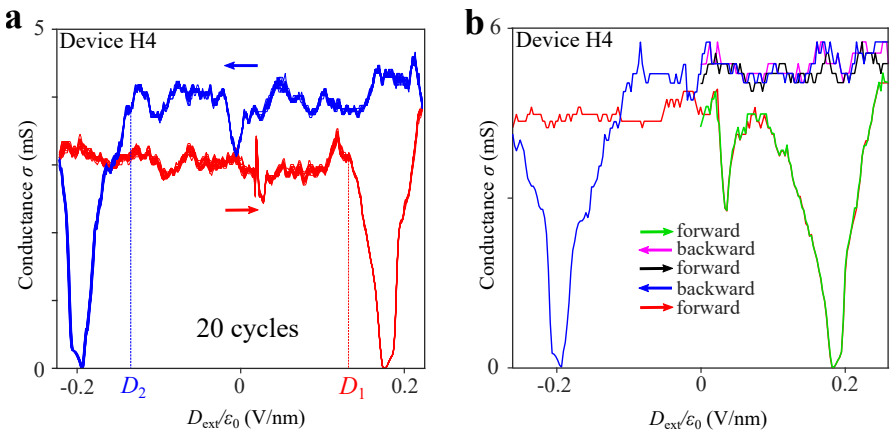

FIG. 4: **Robustness of the ferroelectric switching in the graphene/BN moiré system. a,** Measurements of the conductance at $n_{\text{ext}} = 0$ for forward and backward sweeps of D_{ext} (repeated 20 times). **b,** Consecutive measurements of conductance as a function of D_{ext} with alternating forward and backward scan directions (denoted by the colored arrows) and for different scan ranges.

Methods

Device fabrication and rotational alignment: We fabricated BN-encapsulated Bernal-stacked bilayer graphene devices with different alignment configurations between graphene and BN. Graphene and BN flakes were first exfoliated onto Si/SiO_2 chips. Bilayer graphene was identified using Raman spectroscopy. BN flakes with suitable thicknesses (between 10 to 50 nm) were chosen based on optical contrast and later measured by atomic force microscopy. In addition, we chose graphene and BN flakes with long and straight edges, which, with high likelihood, correspond to one of the crystallographic axes (armchair or zigzag). Therefore, the straight edges can be used as a guide for rotational alignment between different flakes. The bottom BN, graphene, and the top BN flakes were stacked together and transferred onto pre-patterned metal bottom gates through the standard dry-transfer technique using a polydimethylsiloxane (PDMS)/poly(bisphenol A carbonate)(PC) stamp. In Devices H1, H2, and H3, the top and bottom BN were from two independent flakes. We intentionally aligned the straight edges of only the top BN (for H1 and H3) or both the top and bottom BN (for H2) to that of graphene. In Device H4, we used the reactive ion etching (RIE) method to cut one large BN flake into two pieces and used them for both the top and bottom BN layers. The straight edges of top and bottom BN (originally the same edge in this case) and graphene were all aligned for Device H4. Electrical connections to the devices were made through a top contact method: we first used electron beam lithography to define electrode areas, then etched the top BN within those areas and evaporated Cr/PdAu on top of the now exposed graphene. In some of our devices, a protective layer of BN was transferred on top of the device before the top gate (metal or monolayer graphene) was fabricated (details specified in Extended Data Table 1). In the dual-gate (top gate voltage V_{TG} and bottom gate voltage V_{BG}) structure, the externally injected carrier density, n_{ext}, is defined as $n_{\mathrm{ext}} = \frac{\varepsilon_{\mathrm{b}}\varepsilon_0 V_{\mathrm{BG}}}{e d_{\mathrm{b}}} + \frac{\varepsilon_{\mathrm{t}}\varepsilon_0 V_{\mathrm{TG}}}{e d_{\mathrm{t}}}$ and the externally defined displacement field, $D_{\mathrm{ext}} = \frac{1}{2}(\frac{\varepsilon_{\mathrm{b}}\varepsilon_0 V_{\mathrm{BG}}}{d_{\mathrm{b}}} - \frac{\varepsilon_{\mathrm{t}}\varepsilon_0 V_{\mathrm{TG}}}{d_{\mathrm{t}}})$. $D_{\mathrm{ext}}/\varepsilon_0$ is the effective electric field applied to the bilayer graphene through the combination of the top and bottom gates, following many of the previous studies [39, 44, 47, 48]. Here, ε_0 is the vacuum permittivity, $\varepsilon_{\mathrm{b(t)}}$ is the bottom (top) gate dielectric constant, and $d_{\mathrm{b(t)}}$ is the thickness of bottom (top) BN flake. In Devices H2 and H4, however, the prominent hysteretic behavior imposes challenges on the conversion based on the definition above. Therefore, we define n_{ext} and D_{ext} based on the Hall density measurement and the resistance peak slope in the dual-gate map in the

"normal bilayer graphene" region. For the same device, we keep a constant conversion for all the data presented.

We performed optical second-harmonic generation (SHG) measurements to determine the crystallographic axes of BN [49] and therefore the relative rotational angles between the top and bottom BN flakes for Devices H1, H2 and H3. The measurements (SI.V.1) show that for Devices H1 and H3, the top and bottom BN are rotated by $\sim 20^\circ$ (or 80°). For Device H2, the top and bottom BN were rotated by $\sim 30^\circ$ (or 90°). This is not surprising, as the straight edge can be along either the zigzag or armchair direction in honeycomb lattices. In Device H4, the top and bottom BN originate from the same flake. However, the relative alignment angle between the top and bottom BN can still be 0° or 180°. This is because of BN crystal's natural stacking sequence: each BN layer is 180° rotated with respect to its neighbor. Therefore, depending on the evenness or oddness of the number of layers of the BN flake, the two BN layers that directly interface with the bilayer graphene can have a relative angle of 0° or 180°. This angle certainly can affect the top and bottom moiré patterns, which in turn affect the moiré band structure. However, they cannot be distinguished by our current fabrication and deserve future investigation.

For Devices H1 and H3, we can extract the moiré wavelength and twist angle between graphene and BN from the carrier density at the superlattice gaps, which correspond to the full filling of the moiré bands (4 electrons per moiré unit cell). The moiré wavelength λ and the twist angle ϕ are related to the superlattice density n_s as follows [50]:

$$\lambda = \frac{(1+\delta)a}{\sqrt{2(1+\delta)(1-\cos\phi)+\delta^2}}\ , \qquad \frac{g_s g_v 2}{\sqrt{3}\lambda^2} = n_s$$

where a is graphene lattice constant, δ is the lattice mismatch between BN and graphene, and g_s and g_v are the spin and valley degeneracies. Due to the lattice mismatch, it has been previously shown that the graphene/BN superlattice with both zero or small twist angles can give rise to a moiré pattern with long wavelength [50–54]. For both H1 and H3, the moiré wavelength is $\sim$ 10 nm, corresponding to a twist angle $\sim 1^\circ$. For Devices H2 and H4, it is difficult to identify superlattice peaks due to the prominent hysteretic behavior of carrier density with gating (See SI. V for more information).

Summary of device parameters and basic behavior: We have measured a spectrum of different dual-gated graphene devices, including monolayer graphene (MLG), Bernal-

stacked bilayer graphene (BLG), and ABA trilayer graphene (TLG) with various alignment configurations to the top and bottom BN. Among these devices, we only observed significant hysteretic behavior with the displacement field in aligned BLG devices. In these devices, the BLG and the top and/or bottom BN are stacked with special angles. Parameters of hysteretic devices and representative control devices are summarized in Extended Data Table 1 and further explained in the text below. Here, we use M for monolayer, N for normal bilayer, T for trilayer, and H for hysteretic devices:

To further illustrate the behavior of different devices and compare their responses to the out-of-plane displacement field, we highlight some of the key devices in Extended Data Fig. 1.

1. **Device M1**: In panels **a-c**, we show the behavior of a double-aligned monolayer graphene device. The resistance map is characterized by insulating regimes (high resistance) along the top-left to bottom-right diagonal line with multiple series of superlattice peaks corresponding to different moiré wavelengths due to the close alignment of all three components. No hysteresis is observed as we sweep the displacement field back and forth.

2. **Device N0**: In panels **d-f**, for the un-aligned bilayer graphene Device N0, we indeed observe the normal bilayer graphene transport behavior, as observed in many previous studies [47, 55]. The resistance map is characterized by insulating regimes (high resistance) along the top-left to bottom-right diagonal line with a displacement field dependent gap-opening behavior but metallic regimes (low resistance) elsewhere. No hysteresis is observed as we sweep the displacement field back and forth.

3. **Device T1**: In panels **g-i**, we show the behavior of an aligned trilayer graphene device. Instead of a gap-opening behavior along the displacement field, we note that the high resistance area is near the zero displacement field region and decreases as the displacement field increases. This is consistent with what is reported for the case of ABA stacked trilayer graphene [56, 57]. As with the normal bilayer graphene, we do not see an obvious sign of hysteresis when we scan along the displacement field direction.

4. **Device H1/H3**: Devices H1 and H3 have the same stacking configurations between

the BLG and BNs and exhibit the same hysteretic characteristics. We show measurements from Device H1 in panels **k-m**. The resistance of the Dirac peak is asymmetric about the zero displacement field. Depending on the scanning direction, the resistance in the positive displacement field side is higher (or lower) than that in the negative displacement field side. This hysteretic behavior is better visualized in panel **m**, where the forward and backward curves form a closed hysteresis loop.

5. **Device H2/H4**: We classify Devices H2 and H4 in the same group with strong hysteresis. "Strong" means: (a) There exists striking switching between "normal dual gating" and "layer-specific anomalous screening" (LSAS) regimes. In the LSAS regime, the resistance peak runs parallel to a single gate in the dual-gate map (panel **o**). (b) In the $n-D$ map (panel **p**), between the forward and backward displacement field scans, the resistance peak lines have a significant shift in terms of externally defined carrier density; (c) In both the dual-gate $V_{\rm BG}-V_{\rm TG}$ map and $n-D$ map, there is dramatic asymmetry both between $+D$ and $-D$ and between electron and hole. (a),(b) and (c) are closely linked. The strong hysteretic behavior is the focus of our analyses in the paper.

Distinguishing the intrinsic and extrinsic mechanism: Below, we discuss the possibility that our observations, including the strong hysteresis and the LSAS phenomena, are caused by trapped extrinsic charges. Of particular importance is to address the possibility of extrinsic charge injection into the bilayer graphene system by the applied gate voltages. We consider two possible extrinsic trapping sites: defects in the BN dielectrics and at the graphene/BN moiré interfaces. They are both unlikely due to the following experimental facts: (1) Let us assume that the hysteresis arises from extrinsic charges in a particular BN layer (*e.g.*, the bottom BN). Given the fact that the bilayer graphene is electrically grounded, the top gate voltage $V_{\rm TG}$ will not be able to apply any significant electric field in the bottom BN dielectric. In other words, the switching, in this case, will only depend strongly on $V_{\rm BG}$ but will be nearly independent of $V_{\rm TG}$. In contrast, in our data, the switching depends on $D_{\rm ext}$, which is accomplished by scanning $V_{\rm TG}$ and $V_{\rm BG}$ in a coordinated manner. This clearly shows that the ferroelectric switching arises from the bilayer graphene itself, rather than from defects (charge injections) from the dielectric layer on a single side. (2) We have studied carefully aligned *monolayer* graphene/BN moiré systems and ABA *trilayer* graphene/BN

moiré systems. The results are consistent with previous studies [13, 51–54]. They do not show the hysteresis as observed in Devices H2 and H4. (3) We have studied many bilayer graphene/BN devices (including Devices H1-H4 and additional devices shown in Methods). We fabricated these devices using the same procedures but with various relative alignment angles between the three components (bottom BN, graphene, and top BN). The hysteresis is found to be uniquely tied to the relative alignment angles. (4) In SI.V.2, we present additional data from Device H2, which shows that the hysteresis behavior is indeed sensitive to very small angle variations across the sample. (5) In previous studies, hysteresis caused by extrinsic charge trapping states is found to strongly depend on the gate sweeping rate [58]. In contrast, our measurements (Extended Data Fig. 8) show that the observed hysteresis is independent of gate sweeping rates. In SI.II, we expand on the above discussion and also provide additional pieces of evidence. These systematic measurements and analyses, taken collectively, strongly suggest that extrinsic charge traps are highly unlikely, indicating an intrinsic origin of the observed ferroelectricity.

Our systematic measurements provide important clues towards understanding the microscopic mechanism for the observed ferroelectricity. In conventional ferroelectrics, the ions spontaneously displace in an ordered fashion that breaks crystalline inversion symmetry, leading to an electrical polarization. Such a lattice model is less likely here based on the combination of our theoretical analyses and experimental observations: (1) In a pristine BN-aligned bilayer graphene lattice, no macroscopic electrical polarization is expected. This is because, while boron and nitrogen provide opposite local potentials to carbon, the existence of the moiré pattern leads to cancellation upon spatial average (see analyses in SI.II.2). (2) The sharpness of features in the resistance and capacitance maps (Extended Data Fig. 7), as well as the consistency over many consecutive scans, indicate that the ferroelectric switching is uniform over the entire sample, rather than from local structures on the moiré scale [59]. (3) More importantly, the LSAS behavior is beyond what is expected for conventional ferroelectric materials. In a conventional ferroelectric material, positive and negative bound charges move under the influence of the external displacement field, flipping the polarization. Notably, the displacement field only flips the polarization but does not change the number of total mobile carriers. This is the case for all well-studied ferroelectric materials (being insulators with zero carrier density before and after the switching). This is also the case for the recently discovered ferroelectric metal, few-layer WTe_2. Despite the presence of free

carriers, in WTe_2, the total mobile carrier density remains unchanged before and after the switching via the displacement field [44]. In sharp contrast, here we observe that, because of the LSAS behavior, the displacement field can change the total mobile carrier density of the bilayer graphene, as demonstrated by the Hall measurements.

Understandings on the relation between Device H2 and H4: While the microscopic picture in the main text was described based on Device H4, behaviors in both devices can be understood consistently within the same picture. One noticeable difference in detailed behavior between Devices H2 and H4 is the opposite sequence between normal bilayer graphene and the LSAS regime as we described in the main text. We may understand this difference by assuming that in Device H4 a minimum D_{ext} is needed to generate the flat band, whereas, in Device H2, a layer-specific moiré flat band may be already present close to the Fermi level at $D_{\text{ext}} = 0$. Such an assumption requires that the flatness of the band depends both on the displacement field and the details of the moiré potential, which is quite likely in Bernal bilayer graphene. Indeed, recent experiments on twisted double bilayer graphene show correlated insulator behavior only for intermediate displacement field ranges [15–18]. In our system, the moiré band structure will depend on delicate geometrical properties. One obvious geometrical property is the stacking angle. Another geometrical property relevant in Device H4 is the translational alignment between the two moiré patterns. Because the graphene layers in Device H4 are rotationally aligned with both BN flakes, the moiré patterns from both sides are expected to be very similar in terms of moiré unit cell structure and wavelength. Thus, the translational alignment between the two moiré patterns in Device H4 may be important. In summary, the coexistence and independent configuration of the top-BN/graphene moiré potential and bottom-BN/graphene moiré potential, together with applying an displacement field can fine-tune both the single-particle band structures and the correlation landscape, giving rise to different behaviors in Devices H4 and H2.

Probing the out-of-plane electrical polarization using the monolayer graphene sensor: In Device H4, which has monolayer graphene as its top gate, we can also probe the out-of-plane polarization by using the top monolayer graphene (tp-MLG) as an electric field sensor, a technique demonstrated in Ref. [44]. The monolayer graphene conductance serves as a direct measurement of the electrical field inside the top BN dielectric (E_{t}). To then relate E_{t} to the electrical polarization P (areal polarization density, with unit $\mu\text{C} \cdot \text{cm}^{-2}$) of the bilayer graphene (BLG), we define E_{i} as the interlayer electric field and d_{i} as the

interlayer distance of the BLG. We have the relation $\varepsilon_0\varepsilon_t E_t = \varepsilon_0 E_i + P$ directly following Gauss's law. Further, For the case that the MLG and BLG are both grounded and the BLG is at charge neutrality, we have another relation $E_t d_t + E_i(\frac{1}{2}d_i) = 0$. According to the two relations above, P directly depends on E_t through $P = (\varepsilon_0\varepsilon_t d_i + 2\varepsilon_0 d_t)\frac{E_t}{d_i}$. Since $d_t \gg d_i$, $P \sim 2\varepsilon_0\frac{d_t}{d_i}E_t$. Now, we consider two states of the bilayer with opposite electrical polarizations but with zero net charge. The change of polarization ΔP between these two states is directly proportional to the corresponding changes of the top electric field ΔE_t: $\Delta P \sim 2\varepsilon_0\frac{d_t}{d_i}\Delta E_t$.

As a reference, we first measure the tp-MLG conductance as a function of the gate voltage applied between the BLG and the tp-MLG, V_{BL} (Extended Data Fig. 6**e-f**). This allows us to uniquely assign a corresponding value of E_t to each value of the tp-MLG conductance through the relation $E_t = V_{BL}/d_t$ (V_{BL} can be read from the x-axis) (assuming we know whether the monolayer is electron-doped or hole-doped). Now, we ground both the tp-MLG and the BLG, and measure the monolayer graphene conductance as we vary the bottom gate voltage V_{BG}. As shown in Extended Data Fig. 6**d**, the tp-MLG conductance exhibits a significant hysteresis when we scan V_{BG} forward and backward. Particularly, the tp-MLG shows two different conductance values when the BLG has opposite polarization but remains charge neutral (as a comparison between Extended Data Fig. 6 panel **d** and panel **b** shows). By extracting V_{BL} values corresponding to these two tp-MLG conductance values, we obtain $\Delta P \sim 2\varepsilon_0\Delta V_{BL}/d_i \sim 0.12\ \mu\text{C}\cdot\text{cm}^{-2}$.

This value is on the same order of magnitude as the one obtained from Fig. 3, but the specific value differs by a factor of 2.4. We provide one possible reason for this discrepancy. For simplicity, we refer to the method used in Fig. 3 as Method I and the method used in Extended Data Fig. 6 as Method II. In Method I, ΔP is extracted according to $\varepsilon_0 E_i + P = 0$ (effective displacement field is zero between the top and bottom layers of the BLG) at the gapless point of the BLG. In Method II, ΔP is extracted according to $E_t d_t + E_i(\frac{1}{2}d_i) = 0$, meaning the potential drop between the center of the BLG and the tp-MLG is zero when they are both grounded. Experimentally, the potential at the center of the BLG may not be strictly zero.

Probing the electronic compressibility through capacitance measurements: To further confirm the dramatic hysteretic behavior observed in transport measurements, we also performed capacitance measurements, which are sensitive to the bulk properties of the

entire device area rather than local electronic behavior. Due to the low dimensionality of bilayer graphene, the capacitance measured between the graphene and one of the gates contains a significant contribution from the electronic compressibility, a thermodynamic measure of the density of states. In a 2D system with a single gate, the capacitance is related to the compressibility through a quantum capacitance term, $C_{\rm q} \equiv Ae^2\partial n/\partial\mu$ (A is the area of the capacitor and μ is the chemical potential), which sums in series with the geometric capacitance $C_{\rm g}$ to yield the total capacitance, $C^{-1} = C_{\rm g}^{-1} + C_{\rm q}^{-1}$. In bilayer graphene with top and bottom gates, there is a similar relation for each of the top and bottom capacitances, with additional terms due to the coupling between the layers.

Here, we focus on bottom-gate capacitance data from Device H2, measured in a 4 K He cryostat with an excitation voltage of $\delta V_{\rm BG} = 1$ mV at 57.3 kHz. The off-balance signal from a capacitance bridge (point "(B)" in Extended Data Fig. 7**e**) is amplified using a cryogenic two-stage amplifier to remove the effect of stray capacitances from measurement cabling. The capacitance was calculated by relating the off-balance voltage to a reference capacitance on the bridge circuit.

By measuring the bottom-gate capacitance $C_{\rm b}$ while sweeping the gate-defined displacement field, $D_{\rm ext}$, for a series of fixed gate-defined carrier densities, $n_{\rm ext}$, we directly map the parameters for which the bulk of the bilayer becomes incompressible (dark lines in Extended Data Fig. 7**a**), denoting the opening of a band gap. Normally, in intrinsic bilayer graphene, there is a band gap at charge neutrality that depends monotonically on the magnitude of the displacement field. However, in our experiment, the incompressible feature deviates from $n_{\rm ext} = 0$ for a large range of displacement fields. Sweeping the external field in the opposite direction (Extended Data Fig. 7**b**) results in a large shift in the position of this feature, in good agreement with the shift of the resistive state, observed in transport (Extended Data Fig. 5**a-b**). The hysteretic path of this incompressible state, and the correspondence between capacitance dips and resistance peaks, as shown in Extended Data Fig. 7**c-d**, crucially confirms that the resistance switching behavior observed in transport is a bulk property of the bilayer graphene.

[47] Zhang, Y. *et al.* Direct observation of a widely tunable bandgap in bilayer graphene. *Nature* **459**, 820–823 (2009).

[48] Young, A. F. & Levitov, L. S. Capacitance of graphene bilayer as a probe of layer-specific properties. *Phys. Rev. B* **84**, 085441 (2011).

[49] Li, Y. *et al.* Probing symmetry properties of few-layer MoS_2 and h-BN by optical second-harmonic generation. *Nano Lett.* **13**, 3329–3333 (2013).

[50] Yankowitz, M. *et al.* Emergence of superlattice dirac points in graphene on hexagonal boron nitride. *Nature Phys.* **8**, 382–386 (2012).

[51] Dean, C. R. *et al.* Hofstadter's butterfly and the fractal quantum Hall effect in moiré superlattices. *Nature* **497**, 598–602 (2013).

[52] Ponomarenko, L. *et al.* Cloning of Dirac fermions in graphene superlattices. *Nature* **497**, 594–597 (2013).

[53] Hunt, B. *et al.* Massive Dirac fermions and Hofstadter butterfly in a van der Waals heterostructure. *Science* **340**, 1427–1430 (2013).

[54] Finney, N. R. *et al.* Tunable crystal symmetry in graphene-boron nitride heterostructures with coexisting moiré superlattices. *Nature Mater.* **14**, 1029–1034 (2019).

[55] Novoselov, K. S. *et al.* Unconventional quantum Hall effect and Berry's phase of 2π in bilayer graphene. *Nature Phys.* **2**, 177–180 (2006).

[56] Craciun, M. *et al.* Trilayer graphene is a semimetal with a gate-tunable band overlap. *Nature Nanotech.* **4**, 383–388 (2009).

[57] Jhang, S. H. *et al.* Stacking-order dependent transport properties of trilayer graphene. *Phys. Rev. B* **84**, 161408 (2011).

[58] Wang, H., Wu, Y., Cong, C., Shang, J. & Yu, T. Hysteresis of electronic transport in graphene transistors. *ACS nano* **4**, 7221–7228 (2010).

[59] McGilly, L. *et al.* Seeing moiré superlattices. *arXiv preprint arXiv:1912.06629* (2019).

Data availability: The data that support the plots within this paper and other findings of this study are available from the corresponding authors upon reasonable request.

Competing financial interests: The authors declare no competing financial interests.

Device	Bottom BN thickness [nm]	Top BN thickness [nm]	Top-bottom BN relative angle [°]	Protective BN thickness [nm]	Bottom gate material	Top gate material	Geometry	Hysteresis	LSAS
M1	40	40	~ 0	None	Metal	Metal	Hall bar	No	No
N0	42	42	-	20	Metal	MLG	Hall bar	No	No
T1	11	11	-	15	Metal	MLG	Hall bar	No	No
H1	15.5	38	~ 20	8	Metal	Metal	Flower	Weak	No
H2	25	30	~ 30	15	Metal	Metal	Flower	Strong	Yes
H3	28	32	~ 20	5	Metal	Metal	Hall bar	Weak	No
H4	50	50	~ 0	35	Metal	MLG	Hall bar	Strong	Yes

Extended Data Table. 1: **Device parameters and characteristics for Device M1, N0, T1, and H1-H4.** Protective BN means a big BN piece that is used to cover the entire device before fabricating the top gate. The thicknesses of BN were measured by Atomic Force Microscopy (AFM). The relative angle between the top and bottom BN is measured using optical SHG. For details, please refer to the previous Methods section. Flower shape means a device geometry as shown in Fig. S14. MLG means monolayer graphene.

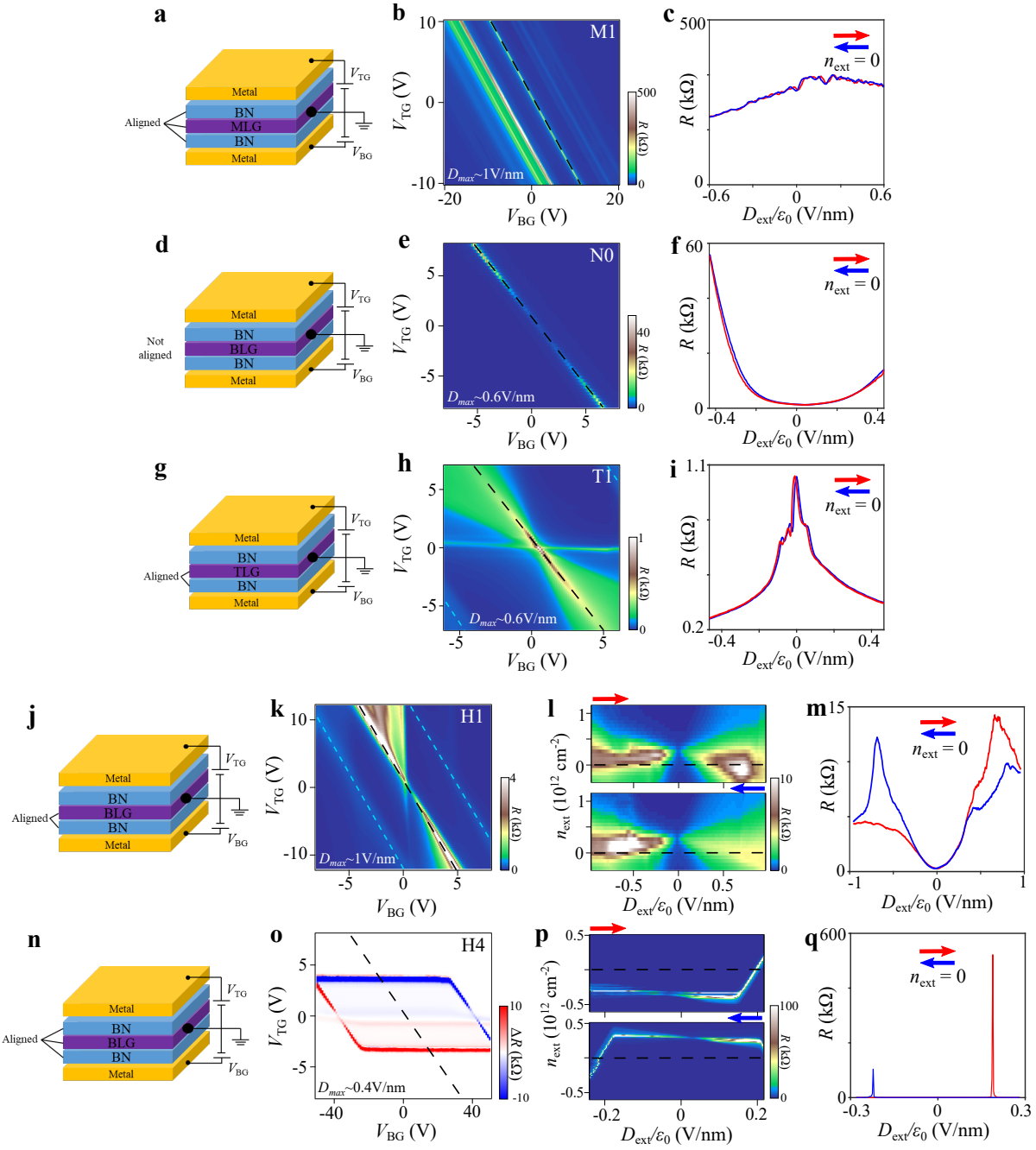

Extended Data Fig. 1: **Resistance data summary for Device M1, N0, T1, H1, and H4.** Device schematic, dual-gate resistance map, $n - D$ map (forward and backward), and resistance as a function of externally applied displacement field at zero doping for representative devices M1 (**a-c**), N0 (**d-f**), T1 (**g-i**), H1 (**j-m**), and H4 (**n-q**). The line traces along the electric field direction are marked by black dashed lines. The superlattice resistance peaks are marked by cyan dashed lines. Note that the horizontal resistance line in **h** stems from a region of the sample that is only controlled by the top gate. Note that line traces in **q** are taken at $n_{\text{ext}} = 0$ from the $n - D$ map (**p**), whereas line traces in Fig. 1**f** in the main text are taken at $V_{\text{TG}} = 0$ from the dual-gate map (Fig. S25**e-f**), hence the difference in resistance magnitude.

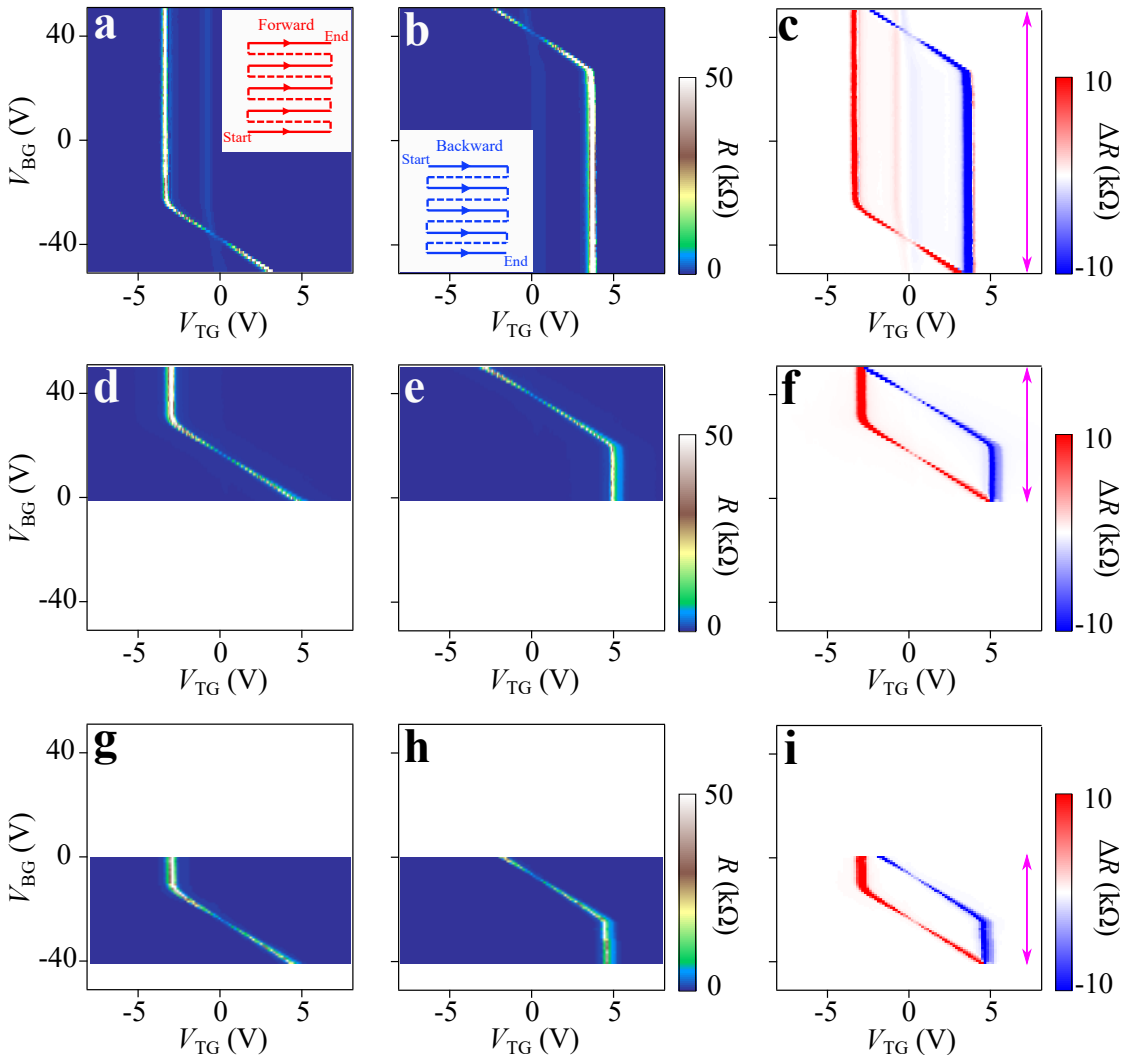

Extended Data Fig. 2: **Shifting of the hysteretic behavior in Device H4. a-c,** Forward (**a**) and backward (**b**) scans of the four-probe longitudinal resistance as a function of V_{TG} and V_{BG} and their difference (**c**). **d-e,** and **g-i,** Same measurements as in **(a-c)**, except that V_{BG} is swept between 0 to 50 V and -40 V to 0, respectively. We present a phenomenological model to simulate the resistance maps in SI.V.3.2.

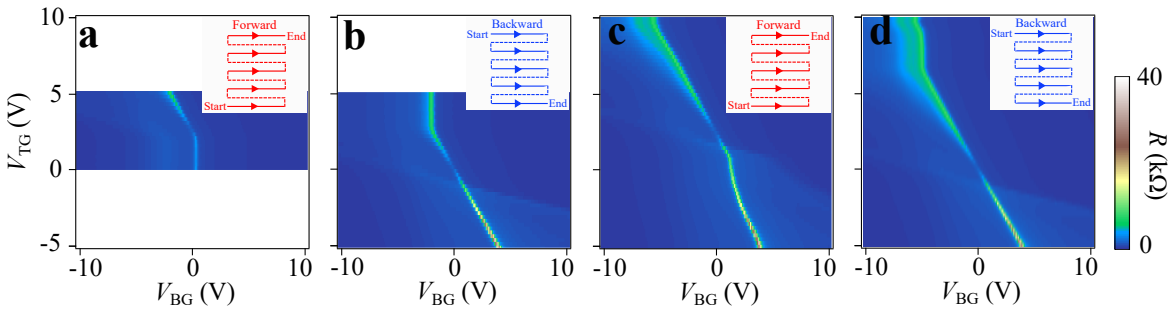

Extended Data Fig. 3: **Hysteretic transport behavior for Device H2. a-d,** The four-probe resistance as a function of V_{BG} and V_{TG}. Scan sequences are shown in the insets.

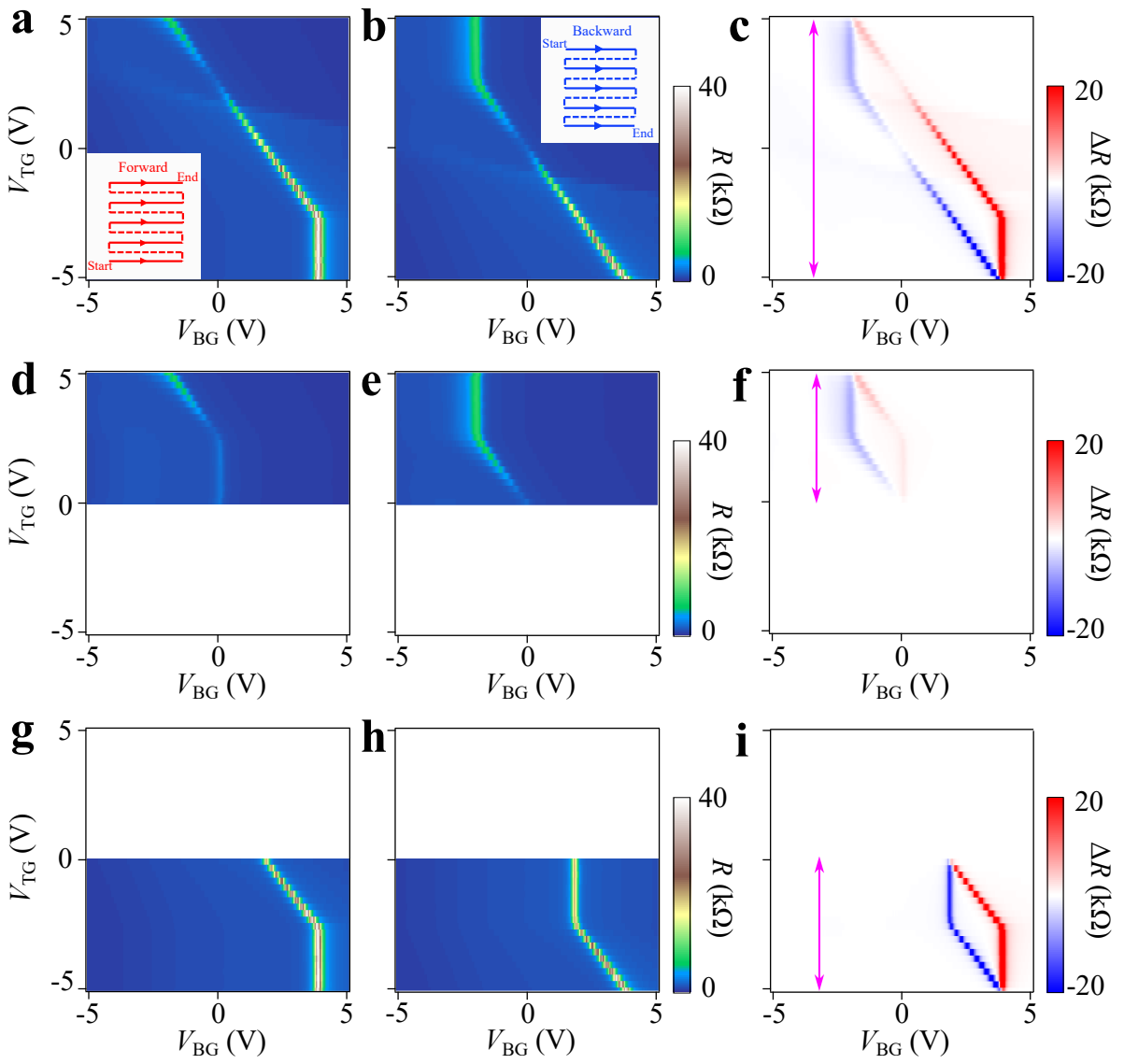

Extended Data Fig. 4: **Shifting of the hysteretic behavior in Device H2. a-c,** Four-probe longitudinal resistance as a function of V_{TG} and V_{BG}. Panels **a**,**b**,**c** show the forward, backward scans and their difference, respectively. **d-f,** and **g-i,** Same measurements as in **(a-c)**, except that V_{TG} is measured within 0 to 5 V and -5 V to 0, respectively.

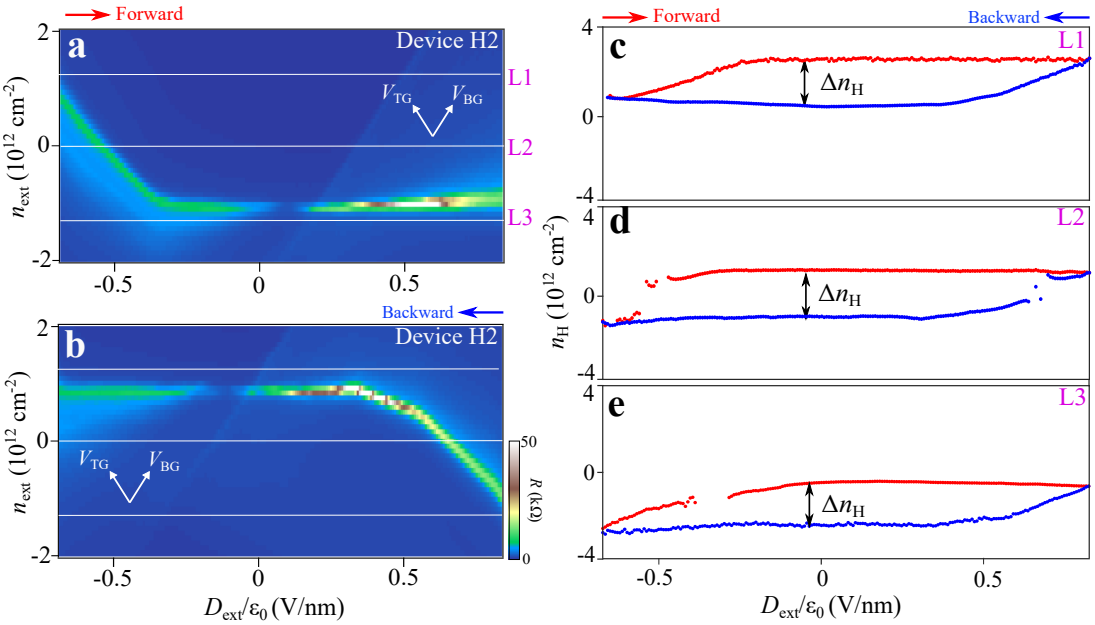

Extended Data Fig. 5: **Hysteretic signature in Hall measurements for Device H2.** The resistance measured while sweeping the externally applied displacement field D_{ext} in the forward (**a**) and backward (**b**) direction at each fixed carrier density n_{ext}. The carrier density scan direction is from the negative to positive values. **c-e,** Carrier density extracted from Hall measurements along the lines denoted in (**a**). Red and blue curves were taken during the forward and backward scan of D_{ext}, respectively.

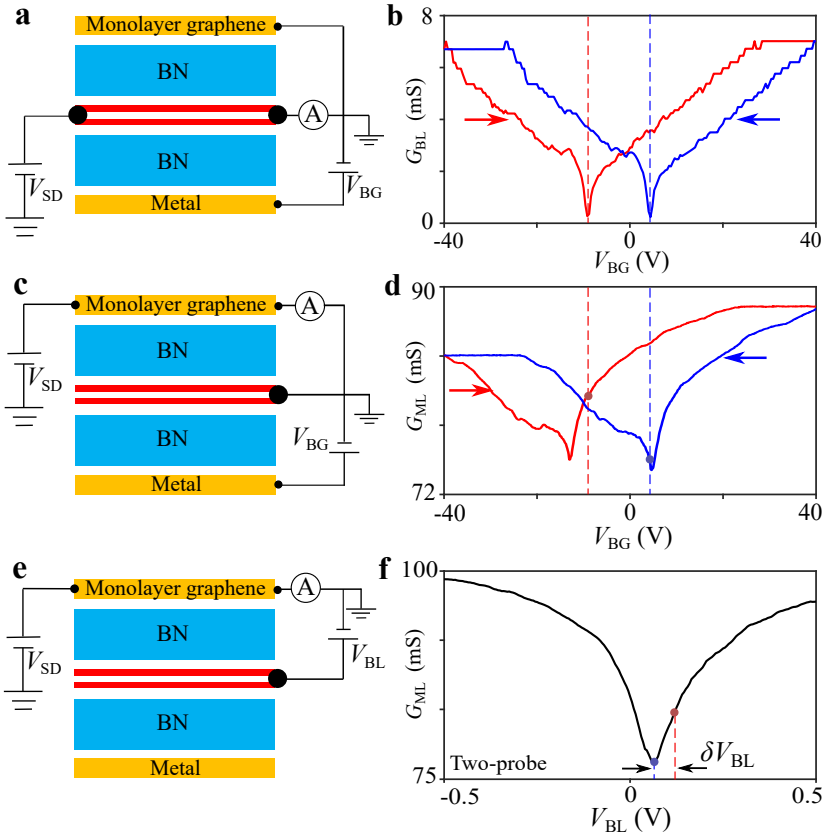

Extended Data Fig. 6: **Probing the out-of-plane electrical polarization using the top monolayer graphene sensor in Device H4. a,** Experimental configuration for measurements of the conductance of the bilayer graphene (BLG). **b,** Measured conductance of the bilayer graphene as a function of V_{BG} (top gate is grounded). The red and blue curves correspond to the forward and backward V_{BG} scans, respectively. The vertical dashed lines denote the V_{BG} values that correspond to the charge neutrality point of the BLG for forward and backward scans. **c,** Experimental configuration for the measurements of the conductance of the top monolayer graphene (tp-MLG). **d,** Measured conductance of the monolayer graphene as a function of V_{BG} with bilayer graphene grounded. The gate voltages are the same as in panel **(b)** (see Methods). The red and blue dots denote the conductance of the tp-MLG when the BLG is charge neutral. **e-f,** Measurements of the conductance of the monolayer graphene as a function of V_{BL} (voltage applied to the bilayer graphene). The conductance of the monolayer at the red and blue dots in panel (**d**) can be inversely mapped to two different V_{BL} values, which corresponds to the difference of electrostatic potentials on the top surface of bilayer graphene induced by ferroelectric switching (see Methods). The in-plane bias voltage V_{SD} was kept below 1 mV for all the measurements.

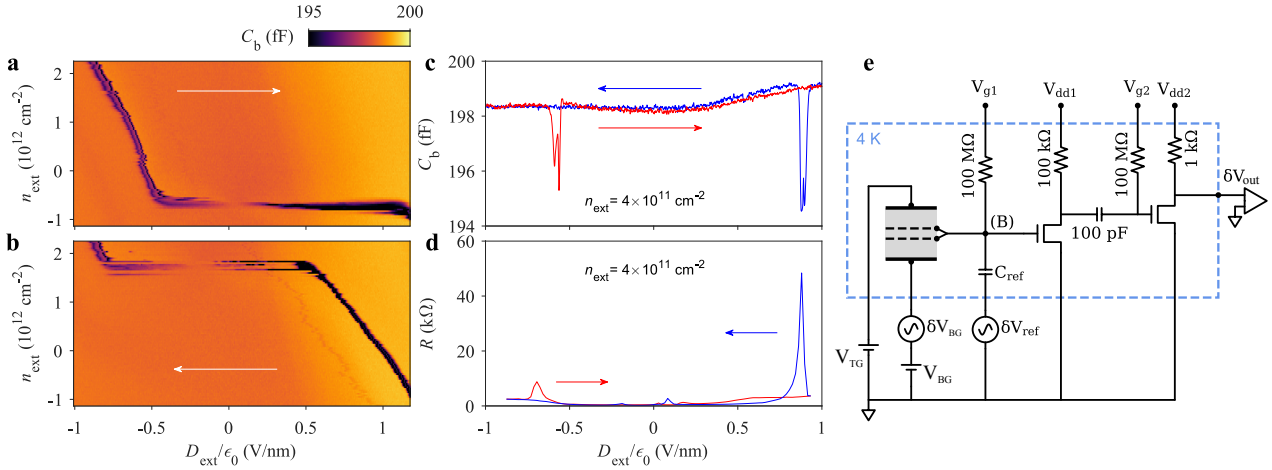

Extended Data Fig. 7: **Hysteresis signature in the bulk electronic compressibility of Device H2. a-b,** Bottom capacitance C_b between the bottom gate and bilayer graphene as a function of the externally applied field, D_{ext} as the fast scan axis, and gate-defined carrier density, n_{ext} as the slow scan axis. The white arrows indicate the sweep direction of D_{ext} in each panel. Deviations of the capacitance from the geometric value reflect modulations in the electronic compressibility, $\partial n/\partial \mu$, from the total area of bilayer graphene overlapping the bottom gate. Data were collected by sweeping the displacement field at each fixed carrier density, as in Figs. 2**h-i**. Dark features indicate regions of incompressibility resulting from the opening of a gap in the bilayer graphene. The gapless point, a compressible state with high C_b, is achieved at a finite D_{ext} that depends on the sweep direction. **c,** Forward and backward traces from (**a**) and (**b**) at a fixed n_{ext}. **d,** Resistance traces at the same density showing resistance peaks corresponding to the incompressible features in (**c**). **e,** Circuit schematic of the bottom gate capacitance measurement, including a two-stage cryogenic amplifier (enclosed in dashed box). Capacitance is measured by applying a small AC excitation voltage to the bottom gate, δV_{BG}, while also applying a nearly 180° out-of-phase signal, δV_{ref}, to a reference capacitor, C_{ref} to null the voltage at the bridge balance point, "(B)". Deviations in the balanced signal caused by variations in compressibility are amplified by two high electron-mobility transistors and measured at the drain of the second stage, δV_{out}. Carrier density n_{ext} and external field D_{ext} are controlled by top- and bottom-gate DC voltages V_{TG} and V_{BG}, in the same way as in the transport measurements.

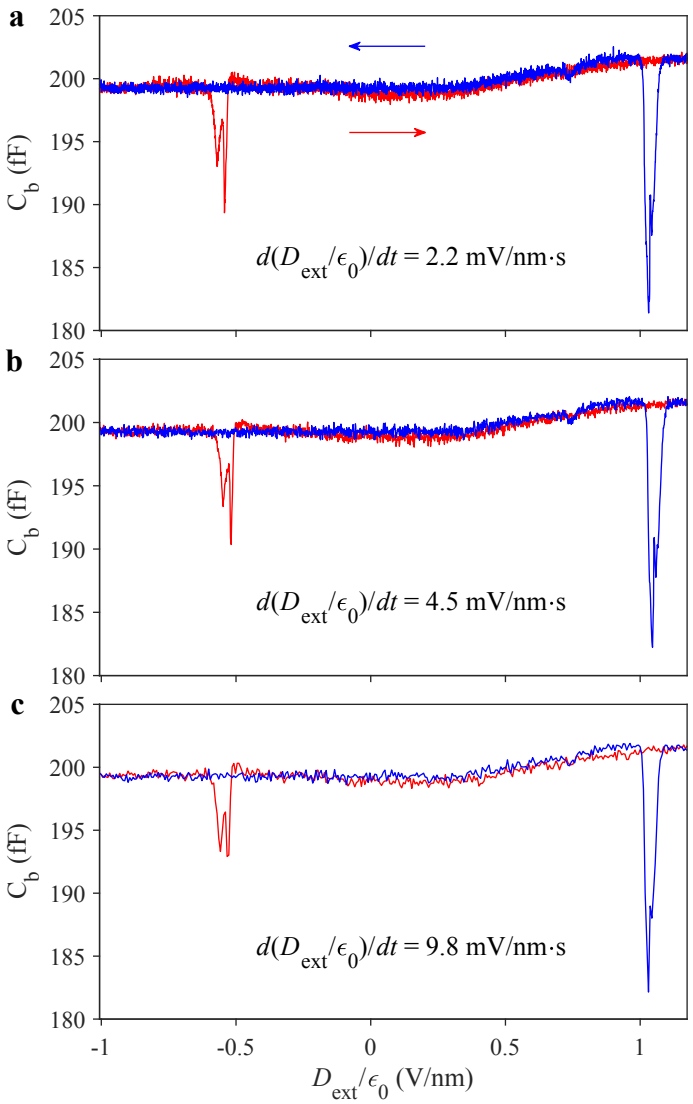

Extended Data Fig. 8: **Independence of the hysteretic behavior on the sweep rate. a-c,** Forward (red) and backward (blue) sweeps of the bottom-gate capacitance, C_b, from Device H2 at fixed carrier density n_ext. Sweep rates shown in each panel denote the rate at which the externally applied displacement field $D_\mathrm{ext}/\varepsilon_0$ was ramped in the BN dielectric layers. No noticeable variation was observed in the capacitance features for a large range of sweep rates from 2.2 mV/nm·s to 9.8 mV/nm·s.